International Global Navigation Satellite Systems Association
IGNSS Symposium 2018

Colombo Theatres, Kensington Campus, UNSW Australia
7 – 9 February 2018

Integrity Monitoring of Vehicle Positioning using Cooperative Measurements under Connected Vehicles Environments

Jiang Liu
School of Civil & Environmental Engineering, University of New South Wales, Australia
School of Electronic & Information Engineering, Beijing Jiaotong University, China
jiangliu@bjtu.edu.cn
Chris Rizos
School of Civil & Environmental Engineering, University of New South Wales, Australia
c.rizos@unsw.edu.au
Bai-gen Cai
School of Electronic & Information Engineering, Beijing Jiaotong University, China
bgcai@bjtu.edu.cn

ABSTRACT

"Trustworthy positioning" is an essential requirement for several safety critical applications of next generation Intelligent Transportation Systems (ITSs), such as automated vehicles and collision avoidance systems. To achieve safe positioning, an information fusion architecture is required to compensate for the drawbacks of GNSS (Global Navigation Satellite System). Different from conventional solutions that integrate navigation assistance sensors such as accelerators, gyroscopes and speedometers, Doppler shift measurements from cooperative neighbourhood vehicles using DSRC (Dedicated Short Range Communication) have shown great potential for cooperative localization and GNSS integrity monitoring. However, the combination of cooperative measurements (GNSS pseudo-range and DSRC carrier frequency offset observables) to detect and exclude existing or potential faults in GNSS is still a challenging issue. In this paper an integrity monitoring method based on the comparison of observed and DSRC-enabled virtual satellite pseudo-range observables is presented for a GNSS/DSRC integrated system operating under connected vehicles environments. Use is made of a road map to construct virtual satellite pseudo-range observables using DSRC range-rates among cooperative vehicles, and the consistency between real and simulated pseudo-ranges is employed in fault detection, identification and exclusion. A system architecture is designed for a DSRC-assisted integrity monitoring scheme. Discussions concerning DSRC range-rate error characteristics are presented backed up by findings from the simulation tests. The results demonstrate that the proposed method is capable of realising cooperative integrity monitoring without relying on additional navigation sensors.

KEYWORDS: Integrity monitoring, Dedicated Short Range Communication, vehicle positioning, cooperative intelligent transportation system.

1. INTRODUCTION

The last three decades have seen steadily increasing research efforts, both in academia and in industry, towards developing driverless vehicle technology (Paden et al 2016). The self-driving and automated technologies have great potential in increasing traffic efficiency, operational safety, personal mobility, and at the same time reducing travel time, fuel use and air pollution. The first task of autonomous driving is accurate and reliable self-positioning. There are many solutions for position determination, however GNSS (Global Navigation Satellite System) is a favoured option due to its many advantages. Nevertheless, even the most accurate GNSS positioning technique using RTK corrections, inertial sensors-based fusion, or sophisticated schemes utilising multi-measurements in vehicular networks cannot completely satisfy the requirements for trustworthy positioning in dense urban environments (Vivacqua et al 2017). In addition to the considerations concerning availability of GNSS signals and services, GNSS integrity must be assured to the required navigation performance for autonomous vehicles (Meng et al 2018). A higher level of integrity is required for highly automated driving, which means certain specified performance parameters must be satisfied, such as integrity risk level and the time to alert, implying an ability to provide timely and correct alerts when a system must not be used (e.g. Worner et al 2016; Karlsson et al 2017). Compared to GNSS integrity augmentation systems, a RAIM (Receiver Autonomous Integrity Monitoring) solution makes it possible to monitor the integrity status of GNSS positioning without relying on ground stations or satellite augmentation signals when operating under complex and uncertain road environments.

Although there have been many RAIM solutions proposed for vehicle navigation and related systems, constraints still exist due to the sometimes unsatisfactory satellite measurement quality and/or insufficiency of satellite visibility. By introducing additional sensor measurements to assist integrity monitoring, such as from INS (Inertial Navigation System) and map database (e.g. Zhong et al 2017; Gu et al 2017), a positioning system is capable of utilising GNSS measurements safely even when a limited satellite visibility leads to failures in GNSS-alone positioning. Recently, there has been an increasing focus on DSRC (Dedicated Short Range Communication) cooperative vehicle positioning (e.g. Alam et al 2013; Shen et al 2016). Introducing DSRC-derived measurements into a RAIM solution, with a framework that was proposed (Ansari 2015), brings substantial benefits in terms of the complexity of the positioning system and the availability of integrity monitoring under VANET (Vehicular Ad-Hoc Network) conditions. In this paper, a DSRC/map-assisted autonomous integrity monitoring methodology is proposed, that does not rely on additional on-board sensors.

The rest of the paper is organised as follows. The principle of DSRC measurements for positioning is briefly introduced in Section 2. Details of the GNSS integrity monitoring algorithm assisted by DSRC are presented in Section 3. Section 4 details the simulation results and presents a discussion on various influencing factors. Finally, Section 5 concludes this paper.

2. PRINCIPLE OF DSRC-BASED VEHICLE POSITIONING

Under VANET environments, neighbourhood vehicles equipped with DSRC units, which cooperate with a specific subject vehicle, can be regarded as moving referencing nodes to

enable cooperative positioning of the subject vehicle. Similar to road-side units, the neighbourhood units share the dynamic states via DSRC wireless packages. Doppler shifts during the message transmission makes it possible to make range-rate measurements for state estimation. To enhance the measurement sets for reliable positioning, road map data is utilised to compute a prediction of the range between a subject vehicle and a neighbourhood vehicle. The principle of cooperative positioning using DSRC is shown in Fig. 1.

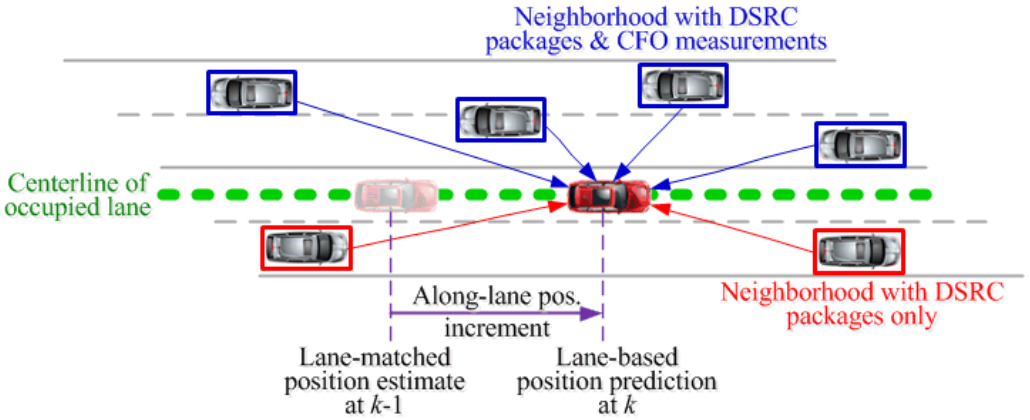

Figure 1. Principle of DSRC-based positioning using cooperative neighbourhood data

The range-rate observable between a DSRC transmitter (in a neighbourhood vehicle) and a DSRC receiver (in a subject vehicle) can be estimated using the Doppler Effect, whereby the CFO (Carrier Frequency Offset) from a DSRC unit is used in a model of the range-rate (Alam et al 2011):

$$\frac{dr}{dt} = c(1-\frac{f_r}{F_t}) = -c(\frac{CFO-\delta_r-\delta_t}{f_t+\delta_t}) \approx -c(\frac{CFO-\delta_r-\delta_t}{f_t}) \tag{1}$$

where $\delta_r = F_r - f_r$ is the clock drift of the receiver, $\delta_t = F_t - f_t$ is the clock drift of the transmitter, F_r is the measured received frequency, f_r is the unknown actual received frequency, F_t is the unknown actual frequency of the transmitter, and f_t is the nominal transmitting frequency. The denominator is simplified since f_t (the typical nominal frequency is 5.9GHz) is much larger than the drift δ_t, and CFO is defined as the difference in frequency:

$$CFO = Measured\ Received\ Freq - Nominal\ Transmit\ Freq = F_r - f_t \tag{2}$$

We can build the measurement model of the CFO measurements from a neighbourhood set to realise the position calculation. A nonlinear function is adopted to describe the relationship between the measurement and a state vector, which includes the subject vehicle's coordinate position, and the velocity and clock drift components. A linearised model for the j th node is written as:

$$CFO_j = -\frac{f_t}{c} \bullet \frac{(x-x_j)v_x + (y-y_j)v_y + (z-z_j)v_z}{\sqrt{(x-x_j)^2 + (y-y_j)^2 + (z-z_j)^2}} + \delta_j + \delta_S \tag{3}$$

where (x_j, y_j, z_j), (v_x, v_y, v_z) denotes position and velocity vectors of the j th neighbourhood vehicle, δ_j indicates the clock drift of the device in the j th neighbourhood vehicle, and δ_S represents the clock drift of the device in the subject vehicle. To enhance the measurement sets for position estimation beyond the DSRC-derived range-rates, state prediction based on apriori knowledge within the road map database is possible. Using the road geometry constraints it is possible to perform forward sensor-free state prediction and provide a calibration to the measurement update results. A tightly-coupled integration of DSRC and map data enables an effective reference for GNSS integrity monitoring, and guarantees a safe measurement update by selecting fault-free satellite measurements for the final position calculation and determination.

3. INTEGRITY MONITORING ALGORITHM

3.1 Fault detection, identification and exclusion

The extended GNSS measurement set, including the real and virtual satellite pseudo-ranges, are utilised to estimate the state of a vehicle. Before the estimation results are generated, the integrity status has to be validated in order to ensure the safety and reliability of the final position determination. Different from the ordinary residual-based (RB) or innovation-based (IB) RAIM methods, we consider a tightly-coupled architecture for state estimation using a structural measurement solution for integrity monitoring. A key step is establishing an extended measurement set beyond just the GNSS pseudo-range measurements so as to improve the service availability of GNSS SIS (Signal-In-Space).

When DSRC CFOs and messages are received from cooperative neighbourhood vehicles, the subject vehicle will firstly perform a forward estimation using the CFO-based range-rates and the road map information. Assume there are m_k effective neighbourhood vehicles at instant k, the range-rates between the subject vehicle and the j th neighbourhood vehicle can be modelled as:

$$\dot{r}_j = \frac{dr_j}{dt} = d\left(\sqrt{(x-x_j)^2 + (y-y_j)^2 + (z-z_j)^2}\right)/dt,\ j = 1, \cdots, m_k \tag{4}$$

where (x_j, y_j, z_j) is the coordinate position of the neighbourhood vehicle. To overcome the insufficiency of range-rates $\{\dot{r}_{k,j}\}$ for the forward estimation, the road map data is used to provide apriori knowledge about the vehicle trajectory during a short time interval. A space-constrained "dead-reckoning" calculation is performed for predicting the current position with the last estimate $\hat{\boldsymbol{x}}_{k-1}$, from which ranges $\{r_{k,j}\}$ can be derived according to (4). By combining range and range-rate information into a measurement vector $\boldsymbol{z}_k = [r_{k,1}, \cdots, r_{k,m_k}, \dot{r}_{k,1}, \cdots, \dot{r}_{k,m_k}]^{\mathrm{T}}$, a nonlinear filter is then employed to generate the forward estimate of the vehicle state $\hat{\boldsymbol{x}}_k^*$, which utilises the information from the DSRC measurements and the map data.

The estimate $\hat{\boldsymbol{x}}_k^*$ makes it possible to extend the original GNSS measurement set under limited visibility conditions. Besides pseudo-range measurements from the n_k visible satellites, we can rebuild "virtual pseudo-ranges" for the blocked satellites by using $\hat{\boldsymbol{x}}_k^*$ and

GNSS almanac or ephemeris. Hence with the aid of u_k virtual satellites the extended measurement vector is:

$$\boldsymbol{y}_k = \left[\breve{\boldsymbol{y}}_k \vdots \hat{\boldsymbol{y}}_k\right]^{\mathrm{T}} = \left[\rho_{1,k}, \cdots, \rho_{u_k,k} \vdots \rho_{u_k+1,k}, \cdots, \rho_{u_k+n_k,k}\right]^{\mathrm{T}} \tag{5}$$

where $\breve{\boldsymbol{y}}_k = [\rho_{1,k}, \cdots, \rho_{u_k,k}]^{\mathrm{T}}$ and $\hat{\boldsymbol{y}}_k = [\rho_{1,k}, \cdots, \rho_{n_k,k}]^{\mathrm{T}}$ indicate the sub-vectors representing real and virtual measurements respectively. For integrity monitoring purposes $\breve{\boldsymbol{y}}_k$ is used to predict the n_k real pseudo-ranges in $\hat{\boldsymbol{y}}_k$ and to determine the integrity status through the comparison. Thus, the forward estimation is capable of providing a positive influence to integrity monitoring through a transformed pseudo-range form. Under a standard LS (Least Squares) estimation architecture, the state can be represented as:

$$\hat{\boldsymbol{x}}_k = \hat{\boldsymbol{x}}_k^- + \Delta\boldsymbol{x}_k = \hat{\boldsymbol{x}}_k^- + (\boldsymbol{H}_k^{\mathrm{T}}\boldsymbol{H}_k)^{-1}\boldsymbol{H}_k^{\mathrm{T}}(\boldsymbol{y}_k - \hat{\boldsymbol{y}}_k^-) \tag{6}$$

where the superscript "-" indicates prediction values, and $\boldsymbol{H}_k$ denotes a linearised measurement matrix as $\Delta\boldsymbol{y}_k = \boldsymbol{H}_k\Delta\boldsymbol{x}_k + \boldsymbol{\varepsilon}_k$. Defining a state vector as $\boldsymbol{x}_k = [x_k, y_k, z_k, \Delta t_k]^{\mathrm{T}}$ including the 3D coordinates and receiver clock bias Δt_k, $\boldsymbol{H}_k$ is a $(l_k \times 4)$ matrix that can be written as:

$$\boldsymbol{H}_k = \begin{bmatrix} \breve{\boldsymbol{H}}_k \\ \cdots \\ \hat{\boldsymbol{H}}_k \end{bmatrix} = \begin{bmatrix} \frac{\partial\rho_{1,k}}{\partial x} & \frac{\partial\rho_{1,k}}{\partial y} & \frac{\partial\rho_{1,k}}{\partial z} & 1 \\ \vdots & \vdots & \vdots & \vdots \\ \frac{\partial\rho_{u_k,k}}{\partial x} & \frac{\partial\rho_{u_k,k}}{\partial y} & \frac{\partial\rho_{u_k,k}}{\partial z} & 1 \\ \cdots\cdots & \cdots\cdots & \cdots\cdots & \cdots \\ \frac{\partial\rho_{u_k+1,k}}{\partial x} & \frac{\partial\rho_{u_k+1,k}}{\partial y} & \frac{\partial\rho_{u_k+1,k}}{\partial z} & 1 \\ \vdots & \vdots & \vdots & \vdots \\ \frac{\partial\rho_{l_k,k}}{\partial x} & \frac{\partial\rho_{l,k}}{\partial y} & \frac{\partial\rho_{l_k,k}}{\partial z} & 1 \end{bmatrix}, l_k = u_k + n_k \tag{7}$$

The estimation equation can be re-written as:

$$\hat{\boldsymbol{y}}_{\alpha,k} = \hat{\boldsymbol{y}}_{\alpha,k}^- + \breve{\boldsymbol{H}}_k(\hat{\boldsymbol{x}}_k - \hat{\boldsymbol{x}}_k^-) \tag{8}$$

$$\hat{\boldsymbol{y}}_{\beta,k} = \hat{\boldsymbol{y}}_{\beta,k}^- + \hat{\boldsymbol{H}}_k(\hat{\boldsymbol{x}}_k - \hat{\boldsymbol{x}}_k^-) \tag{9}$$

where $\hat{\boldsymbol{y}}_{\alpha,k} = [\hat{\rho}_{1,k}, \cdots, \hat{\rho}_{u_k,k}]^{\mathrm{T}}$ and $\hat{\boldsymbol{y}}_{\beta,k} = [\hat{\rho}_{u_k+1,k}, \cdots, \hat{\rho}_{l_k,k}]^{\mathrm{T}}$ are sub-vectors of the estimation of $\breve{\boldsymbol{y}}_k$ and $\hat{\boldsymbol{y}}_k$ respectively, and $\hat{\boldsymbol{y}}_{\alpha,k}^-$ and $\hat{\boldsymbol{y}}_{\beta,k}^-$ represent the prediction vectors with similar structures to $\hat{\boldsymbol{y}}_{\alpha,k}$ and $\hat{\boldsymbol{y}}_{\beta,k}$. Considering the referencing function of $\breve{\boldsymbol{y}}_k$, the LS-based state estimation is:

$$\hat{\boldsymbol{x}}_k = \hat{\boldsymbol{x}}_k^- + \breve{\boldsymbol{H}}_k^{-1}(\breve{\boldsymbol{y}}_k - \hat{\boldsymbol{y}}_{\alpha,k}^-) \tag{10}$$

Thus, the prediction of the components of $\hat{\boldsymbol{y}}_k$, which indicate the predicted pseudo-ranges for all the visible satellites, is derived by using the "innovation" in (10) as:

$$\hat{\boldsymbol{y}}_{\beta,k} = \hat{\boldsymbol{y}}_{\beta,k}^- + \hat{\boldsymbol{H}}_k[\breve{\boldsymbol{H}}_k^{-1}(\breve{\boldsymbol{y}}_k - \hat{\boldsymbol{y}}_{\alpha,k}^-)] = \hat{\boldsymbol{y}}_{\beta,k}^- + \boldsymbol{\Omega}_k(\breve{\boldsymbol{y}}_k - \hat{\boldsymbol{y}}_{\alpha,k}^-) \tag{11}$$

where $\boldsymbol{\Omega}_k = \hat{\boldsymbol{H}}_k \breve{\boldsymbol{H}}_k^{-1}$. The residuals for the visible satellites are:

$$\boldsymbol{q}_k = \hat{\boldsymbol{y}}_k - \hat{\boldsymbol{y}}_{\beta,k} = \hat{\boldsymbol{y}}_k - \hat{\boldsymbol{y}}_{\beta,k}^- - \boldsymbol{\Omega}_k(\breve{\boldsymbol{y}}_k - \hat{\boldsymbol{y}}_{\alpha,k}^-) = \hat{\boldsymbol{\varepsilon}}_k - \boldsymbol{\Omega}_k \breve{\boldsymbol{\varepsilon}}_k \tag{12}$$

where $\boldsymbol{q}_k$ is a $(n_k \times 1)$ residual vector, $\breve{\boldsymbol{\varepsilon}}_k$ denote the error components corresponding to the combined measurement error model of $\boldsymbol{y}_k$ as $\boldsymbol{y}_k = \boldsymbol{H}_k \hat{\boldsymbol{x}}_k + \boldsymbol{\varepsilon}_k$.

Based on the residual $\boldsymbol{q}_k$, the consistency between the measurements (from both the real and virtual satellites) and the estimated result (using only the virtual pseudo-ranges based on the DSRC range-rate measurements and road map data) can be used to provide an indication of the integrity status for the available n_k in-view satellites, no matter whether the criterion $n_k \geq 5$ or $n_k \geq 6$ can be satisfied for the fault detection or the fault exclusion task.

Under the fault-free hypothesis, we assume that the measurement error $\boldsymbol{\varepsilon}_k$ follows the Gaussian distribution with zero mean, and the definite variance as $\varepsilon_{k,i} \sim \mathcal{N}(0, \sigma_i^2), i = 1, \cdots, l_k$. Hence, it could be determined that the residual $\boldsymbol{q}_k$ is also a Gaussian vector with a zero mean and the corresponding covariance can be derived according to (12):

$$\boldsymbol{W}_k = E(\boldsymbol{q}_k \boldsymbol{q}_k^{\mathrm{T}}) = E\left\{(\hat{\boldsymbol{\varepsilon}}_k - \boldsymbol{\Omega}_k \breve{\boldsymbol{\varepsilon}}_k)(\hat{\boldsymbol{\varepsilon}}_k - \boldsymbol{\Omega}_k \breve{\boldsymbol{\varepsilon}}_k)^{\mathrm{T}}\right\} = E(\hat{\boldsymbol{\varepsilon}}_k \hat{\boldsymbol{\varepsilon}}_k^{\mathrm{T}}) + \boldsymbol{\Omega}_k E(\breve{\boldsymbol{\varepsilon}}_k \breve{\boldsymbol{\varepsilon}}_k^{\mathrm{T}}) \boldsymbol{\Omega}_k^{\mathrm{T}} = \hat{\boldsymbol{\Lambda}}_k + \boldsymbol{\Omega}_k \breve{\boldsymbol{\Lambda}}_k \boldsymbol{\Omega}_k^{\mathrm{T}} \tag{13}$$

where $\hat{\boldsymbol{\Lambda}}_k$ and $\breve{\boldsymbol{\Lambda}}_k$ are diagonal matrices, $\hat{\boldsymbol{\Lambda}}_k = diag\{\sigma_1^2, \cdots, \sigma_{u_k}^2\}$ and $\breve{\boldsymbol{\Lambda}}_k = diag\{\sigma_{u_k+1}^2, \cdots, \sigma_{l_k}^2\}$. σ_{obs} denotes an effective standard deviation of the measurement error $\boldsymbol{\varepsilon}_k$ using a specific method, such as the ensemble strategy (Margaria et al 2015), to avoid the difficulty of having to identify in advance the time-varying features of satellite measurement sets and their error characteristics. Thus, the covariance of the residual $\boldsymbol{q}_k$ in (13) can be simplified to be $\boldsymbol{W}_k = \sigma_{\mathrm{obs}}^2(\boldsymbol{I} + \boldsymbol{\Omega}_k \boldsymbol{\Omega}_k^{\mathrm{T}})$.

Based on the analysis of the residual error in the fault-free case, it can be found that the condition $\varepsilon_{k,i} \sim \mathcal{N}(0, \sigma_i^2)$ would be changed when a fault exists in one or more satellite measurements. Therefore a test statistic is constructed based on the residual vector $\|\boldsymbol{q}_k\|^2$ normalised by the standard deviation of the measurement error σ_i^2, where $\|\boldsymbol{q}_k\|^2 = \boldsymbol{q}_k^{\mathrm{T}} \boldsymbol{R}_k^{-1} \boldsymbol{q}_k$ follows a central Chi-square distribution with $(l_k - 4)$ degrees of freedom. The expectation of $\|\boldsymbol{q}_k\|^2$ equals zero in the fault-free case, and therefore the standard LS fault detection strategy can be used to compare the test statistic with a specified threshold for a certain hypothesis test,

such as:

$$\begin{cases} T_k = \sqrt{\boldsymbol{q}_k^{\mathrm{T}} \boldsymbol{R}_k^{-1} \boldsymbol{q}_k} \,/\, \sigma_{\mathrm{obs}} < \mathrm{T_H}, \mathrm{H}_0 : \mathit{FaultFree} \\ T_k = \sqrt{\boldsymbol{q}_k^{\mathrm{T}} \boldsymbol{R}_k^{-1} \boldsymbol{q}_k} \,/\, \sigma_{\mathrm{obs}} \geq \mathrm{T_H}, \mathrm{H}_1 : \mathit{FaultDetected} \end{cases} \tag{14}$$

where $\boldsymbol{R}_k$ is the measurement noise covariance which is determined in advance, $\mathrm{T_H}$ denotes a threshold corresponding to the test statistic T_k, which is calculated with a given probability of false alarm p_{FA} according to the central Chi-square distribution:

$$p(T_k^2 < \mathrm{T_H^2}) = \int_0^{\mathrm{T_H^2}} f_{\chi^2_{l_k-4}}(\xi) d\xi = 1 - p_{\mathrm{FA}} \tag{15}$$

The value of p_{FA} is usually specified beforehand for a certain application. Based on the criterion in (14), existing or potential faults would be detected under the given assumption. If a fault is detected using the comparison of T_k and $\mathrm{T_H}$, it is important to identify the fault(s) and isolate the associated measurement(s) from the final state estimation. Different from the global test statistic concerned with the consistency of all the n_k components in the real pseudo-range measurement set, a local test statistic corresponding to a specific satellite can be used for fault identification (Lanca et al 2017). The standardised residual component of each visible satellite is:

$$t_{k,i} = \left| \frac{q_{k,i}}{\sigma_{\mathrm{obs}} \sqrt{W_{k,ii}}} \right|, i = 1, \cdots, n_k \tag{16}$$

where $q_{k,i}$ and $W_{k,ii}$ represent the ith residual component of $\boldsymbol{q}_k$ and the diagonal element of $\boldsymbol{W}_{k,ii}$ respectively. Similar to the global test, the local hypothesis test is employed by comparing each $t_{k,i}$ with its specified test threshold $\mathrm{D_H}$, which is also related to the given false alarm probability p_{FA}. The local hypothesis test criterion is derived according to the assumption about the statistical character of the $t_{k,i}$ is $\mathcal{N}(0,1)$. The false alarm probability is also involved as follows:

$$\begin{cases} t_{k,i} = \left| \dfrac{q_{k,i}}{\sigma_{\mathrm{obs}} \sqrt{W_{k,ii}}} \right| < \mathrm{D_H}, \mathrm{H}_{0,i} : \mathit{FaultFree} \\ t_{k,i} = \left| \dfrac{q_{k,i}}{\sigma_{\mathrm{obs}} \sqrt{W_{k,ii}}} \right| \geq \mathrm{D_H}, \mathrm{H}_{1,i} : \mathit{FaultIdentified} \end{cases}, i = 1, \cdots, n_k \tag{17}$$

Different from a global threshold $\mathrm{T_H}$ for fault detection, the allocated false alarm probability of each observed satellite is an average of p_{FA}, which means a reduced probability of false alarm p_{FA}/n_k is involved in determining the local threshold $\mathrm{D_H}$. Thus, it will be:

$$p(t_{k,i} < \mathrm{D_H}) = \frac{1}{\sqrt{2\pi}} \int_{-\mathrm{D_H}}^{\mathrm{D_H}} e^{-\frac{\xi^2}{2}} d\xi = 1 - \frac{2}{\sqrt{2\pi}} \int_{\mathrm{D_H}}^{\infty} e^{-\frac{\xi^2}{2}} d\xi = 1 - \frac{p_{\mathrm{FA}}}{n_k} \tag{18}$$

Fault identification is based on the threshold derived for a standard normal distribution. If $t_{k,i}$ exceeds its threshold, the corresponding satellite measurement is considered faulty and affects multiple standardised residuals. To realise the fault exclusion operation, the criterion for decision-making regarding fault exclusion is adopted by considering the following conditions:

$$\begin{cases} T_k = \sqrt{\boldsymbol{q}_k^{\mathrm{T}} \boldsymbol{R}_k^{-1} \boldsymbol{q}_k} \,/\, \sigma_{\mathrm{obs}} \geq \mathrm{T_H} \\ t_{k,i} > \mathrm{D_H} \end{cases}, i = 1, \cdots, n_k \tag{19}$$

The local test observes whether the local test statistic corresponding to a specific range source that exceeds a threshold $\mathrm{D_H}$ with the allocated false alarm probability. Thus, the i th pseudo-range measurement should be excluded from the original measurement vector $\boldsymbol{y}_k$, and the remaining components in $\boldsymbol{y}_k$ will be fed into an estimator for the final position determination.

3.2 Availability assurance of integrity monitoring

The availability of the above fault detection, identification and exclusion methodology is driven by the use of virtual satellite measurements. The integrity monitoring "hole" due to insufficient satellite visibility can be avoided since $u_k \geq 4$ is always fulfilled. However, the geometry of the observed satellites also has to be considered when determining the availability of fault detection and exclusion. Using a protection level-based strategy, the evaluation of the HPL (Horizontal Protection Level) bridges the geometry of the "observable" constellation and the availability of FDE (Fault Detection and Exclusion). Under the faulty hypothesis, the distribution of the global test statistic T_k will be the non-central Chi-square distribution $T_k^2 \sim \chi^2_{l_k-4,\lambda}$, where λ denotes the non-central parameter, which is derived with a required missed detection probability p_{MD}:

$$p(T_k^2 < \mathrm{T_H^2}) = \int_0^{\mathrm{T_H^2}} f_{\chi^2_{l_k-4,\lambda}}(\xi) d\xi = p_{\mathrm{MD}} \tag{20}$$

To evaluate the influence of a fault which is extremely difficult to be detected, we can use the difference of HDOP δd_i, between the whole available constellation (with l_k satellites) and a sub-set where one of the actually visible satellite (within n_k satellites) is removed, to calculate the protection level by considering the effect from the virtual satellites. The difference is:

$$\delta d_{k,i} = HDOP_{k,i} - HDOP_k, i = 1, \cdots, n_k \tag{21}$$

where $HDOP_k = \sqrt{\Sigma_{k,11} + \Sigma_{k,22}}$, $HDOP_{k,i} = \sqrt{\Sigma^{(i)}_{k,11} + \Sigma^{(i)}_{k,22}}$, $\Sigma_{k,jj}$ and $\Sigma^{(i)}_{k,jj}$ are the j th element of $\boldsymbol{\Sigma}_k = (\boldsymbol{H}_k^{\mathrm{T}} \boldsymbol{H}_k)^{-1}$ and $\boldsymbol{\Sigma}_k^{(i)} = ((\boldsymbol{H}_k^{(\mathrm{i})})^{\mathrm{T}} \boldsymbol{H}_k^{(\mathrm{i})})^{-1}$, and $\boldsymbol{H}_k^{(\mathrm{i})}$ denotes a reduced matrix by removing the i th row from its root matrix $\boldsymbol{H}_k$. With a maximum $\delta d_{k,i}$ and the non-central parameter λ,

the HPL can be evaluated as:

$$HPL_k = \sigma_{\text{obs}} \times \sqrt{\lambda} \times \max_i(\delta d_{k,i}), i = 1, \cdots, n_k \tag{22}$$

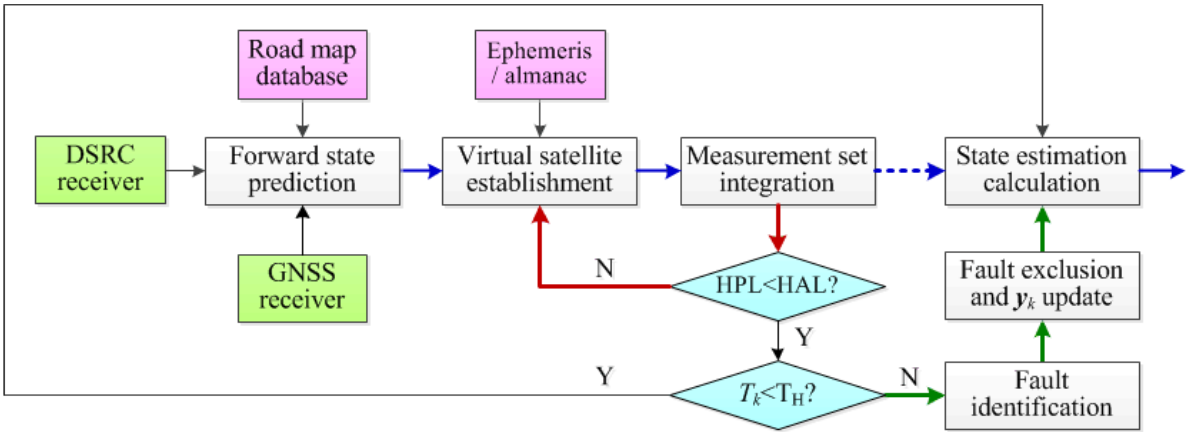

Figure 2. Procedure of the DSRC-assisted GNSS integrity monitoring

By comparing HPL with a specific HAL (Horizontal Alert Limit), the availability of integrity monitoring can be evaluated. Furthermore, the result provides an indication of the effectiveness of the virtual satellite measurements. If HPL exceeds the HAL, re-establishment of the virtual measurement set with different u_k satellites will be required until the criterion $HPL<HAL$ is fulfilled. By considering the availability evaluation and FDE jointly, the entire integrity monitoring process is illustrated in Fig. 2.

3.3 Discussions on influencing factors

Firstly, the performance of DSRC-based forward state estimation for generating the extended measurement set has a major influence on the effectiveness of FDE. It can be found that an estimation $\hat{\boldsymbol{x}}_k^*$ using both the DSRC range-rate measurements and road map database is assumed to be an equivalent LS-based process using u_k virtual satellite pseudo-range measurements, as the decomposition of $\boldsymbol{H}_k$ in (7). Therefore, several issues influence the forward estimation, including the clock synchronisation errors between the subject vehicle and its neighbourhood vehicles, the position errors of the neighbourhood vehicles, latency in wireless message transmission, and the noise characteristics of CFO observations. Hidden assumptions for an estimator, like the nonlinear cubature Kalman filter, also have to be noted, where conditional densities in Bayesian filter frame are assumed Gaussian and fixed measurement noise parameters have to be determined in advance. Furthermore, the resolution and precision of the road map data are also important for addressing the insufficiency of DSRC range-rate measurements in accurate forward estimation.

Secondly, the FDE method inherits the basic framework of the range comparison method using the LS-based structure. A linear measuring matrix $\boldsymbol{H}_k$ is adopted to narrow the gap between the integrity monitoring architecture and the practical situation of the nonlinear measurement model, although the fault-free measurements ensured by FDE are fed to the nonlinear filter for the final state estimation. The approximation error of the standard deviation σ_{obs} and the linearisation error in approximating $\boldsymbol{H}_k$ result in risks of false alarms and missed detection. In addition, the assumptions concerning the nature of the distribution in

residual errors and test statistics also lead to negative effects on integrity monitoring, especially for the situation where uncertainties exist and assumptions with predefined p_{FA} and p_{MD} fail to match reality.

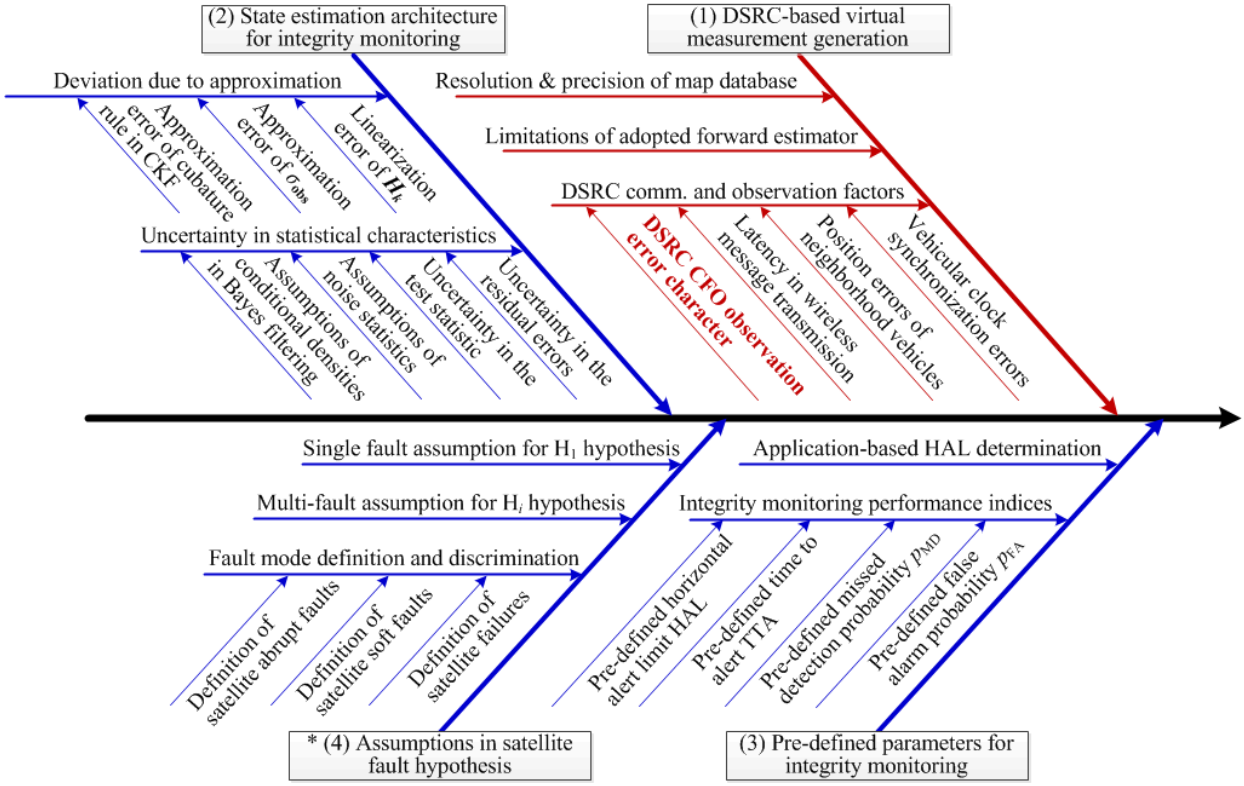

Figure 3. System architecture of the influencing factors in DSRC-assisted integrity monitoring

Thirdly, it is important to determine the integrity monitoring parameters such as HAL, p_{FA}, p_{MD}, required integrity risk level c_{IR} and the time to alert (TTA). Parameters derived from different applications may vary greatly. For example, an extremely small p_{MD} and a much lower HAL have to be adopted for safety-related vehicle operation scenarios, such as collision prevention of self-driving cars, compared to other non-safety-critical GNSS-based applications. With different integrity parameters, the availability of integrity monitoring and the correctness of excluding the biased satellite measurements would be significantly affected.

Furthermore, it should be noted that the definition of fault mode and the adopted hypothesis in fault detection also impacts on the performance of availability evaluation and FDE. In this paper we consider the abrupt fault (jump fault) or the soft fault case. Only the single fault hypothesis is adopted in building a global test statistic. An architecture system of influencing factors for the proposed cooperative integrity monitoring methodology is given in Fig. 3. To illustrate the feasibility and performance of integrity monitoring using the DSRC range-rate-based results, specific attention is given to the characteristics of DSRC range-rate errors, which may be constrained by available DSRC techniques and in-vehicle device products.

4. SIMULATIONS AND DISCUSSIONS

In order to better understand the performance of the proposed integrity monitoring methodology using DSRC data, simulations were performed for scenarios in which a subject vehicle cooperates with other neighbourhood vehicles under VANET conditions. A traffic

simulation tool was used to generate a dynamic traffic situation, and trajectories of the subject vehicle and its neighbourhood vehicles were recorded for the off-line fusion of the GNSS and DSRC measurements. The operation of the subject vehicle between two adjacent intersections, which typically lasts about 90 seconds, is investigated. Satellite measurements were generated by a simulator. Due to the lack of visibility, whereby only four GPS satellites (PRN= 14, 32, 25, 31) were observed during the trip, we use four virtual satellites to enhance the availability for integrity monitoring by using ephemeris data of these unobservable satellites (PRN=18, 22, 10, 12). Based on the results from field experiments, the error of DSRC range-rate measurements are assumed to be Gaussian with $\mathcal{N}(0, 6.5)$. The standard deviation of satellite measurement errors is assumed to be $\sigma_{\text{obs}} = 3.0\,\text{m}$ for generating both the measurement noise covariance for state estimation and the test statistics for integrity monitoring.

An abrupt fault is injected into the original measurements of satellite PRN=14 from *t*=51s to *t*=80s, of step magnitude 50m. In addition the soft fault in satellite PRN=25 was simulated using a ramp error with a velocity of 1m/s from *t*=31s. Hence a two-fault case exists during the period [51s, 80s], which is expected to be identified by the global and local statistics. According to the proposed integrity monitoring methodology, a global test statistic is monitored and four parallel local statistics are evaluated with time. The probabilities of false alarm and missed detection are set as $p_{\text{FA}} = 1\times10^{-5}$ and $p_{\text{MD}} = 1\times10^{-4}$ respectively. During a single run, the time-varying test statistics are shown in Fig. 4. Fig.5 depicts the position errors to illustrate the effect of fault exclusion based on the fault identification results in Fig. 4.

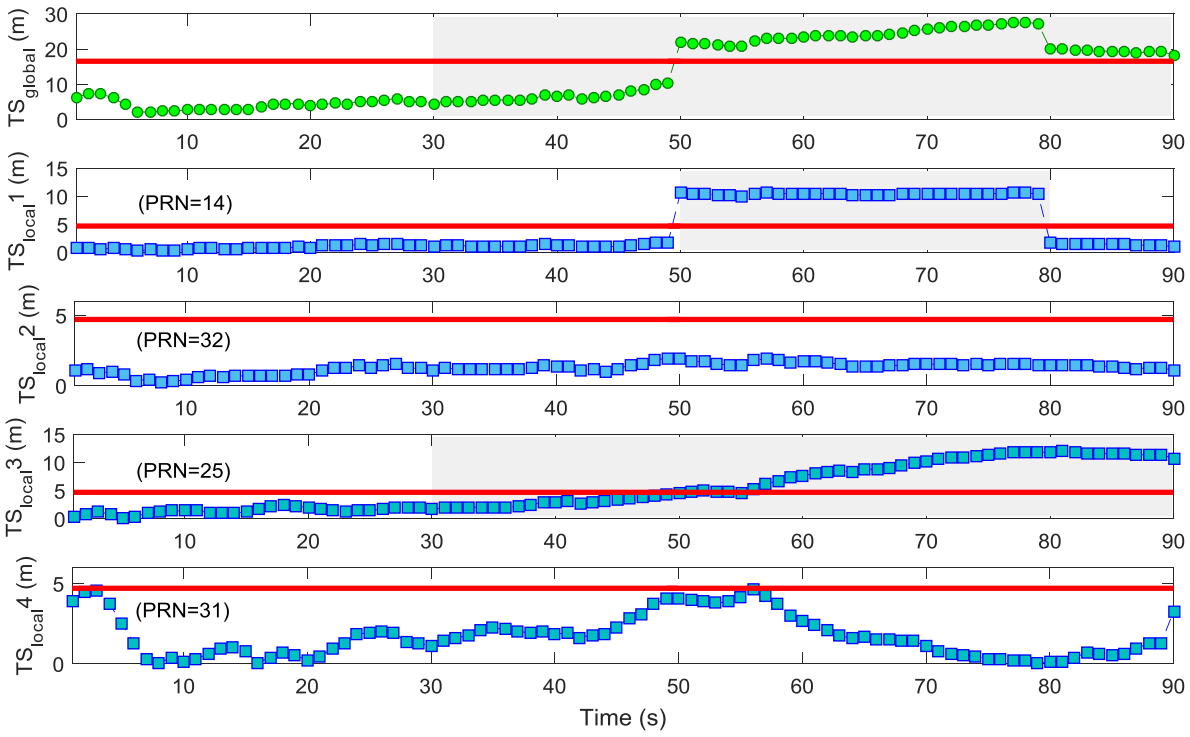

Figure 4. Global and local test statistics for fault detection and identification

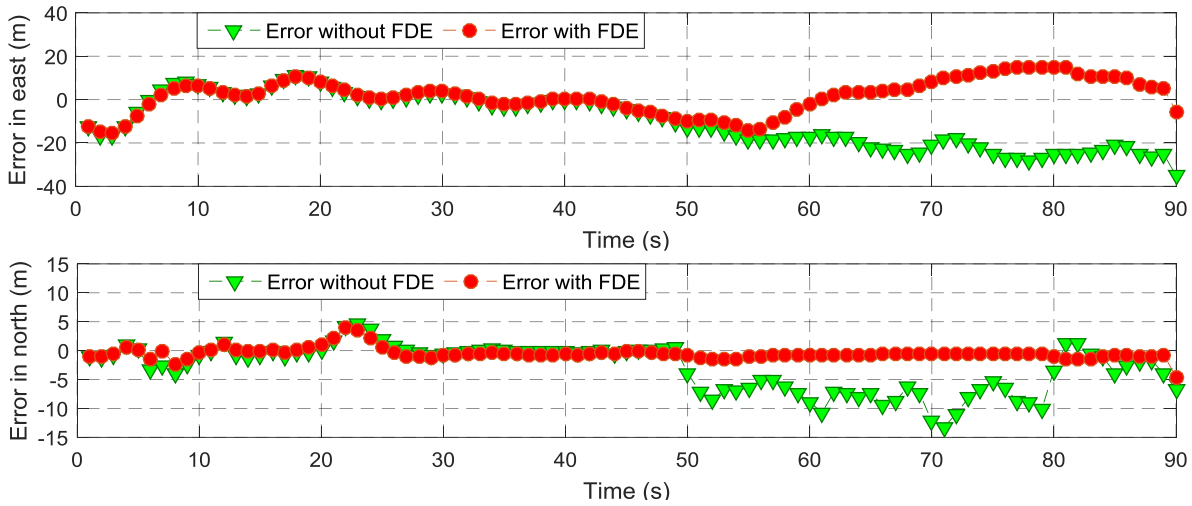

Figure 5. Comparison of position estimation errors under different FDE conditions

From the figures it can be seen that the local test statistics corresponding to the satellites PRN =14 and PRN=25 provide correct indications of the faults. Faults are identified based on the fault detection result, although there is a delay from the beginning of the injected ramp fault and the actual detection point. Compared to the errors without FDE, the horizontal error components are constrained to a certain level by isolating the satellite measurements with identified faults. This cannot be realised using traditional RAIM methods due to insufficient satellite visibility.

To further examine the performance of the DSRC-enabled GNSS integrity monitoring under a given scenario, different assumptions about the STD of the DSRC range-rate error are adopted. Typical STD values are utilised with specific ratios to its basic value as $\sigma_{\text{DSRC}} = 6.5\kappa$, where the ratio κ ranges from 0.1 to 1.0. For each STD assumption 500 runs were carried out for statistical analysis. Fig. 6, Fig. 7 and Fig. 8 show the false alarm and missed detection results when we set $\kappa = 1.0$, $\kappa = 0.6$ and $\kappa = 0.2$ respectively. The percentage of missed detection was investigated separately, where the subscripts (S) and (R) in the label of the vertical axis represent the abrupt fault and soft fault case respectively. It is obvious that fewer false alarms and missed detections of the abrupt faults occur when a smaller STD is used. However, it is found that the soft fault is relatively difficult to detect and identify in the early stages, as the slowly-growing ramp error has not reach the detection capability of the FDE method.

Fig. 9, Fig. 10 and Fig. 11 illustrate the mean values and standard deviations of the position error for the three STD assumptions. From the errorbar plots it is obvious that errors in north direction are more sensitive to the variation of σ_{DSRC}, and there is not too much influence to the error level when the FDE is adopted, even if higher quality DSRC range-rate measurements are assumed in the simulations. For more details about the effect of σ_{DSRC}, statistical results of the average percentages of FDE, during each 500 independent simulation run for different σ_{DSRC} ratios, are summarised in Fig. 12 and Table 1, where κ changes from 10% to 100%. For each σ_{DSRC} assumption the diagonal elements in the measurement noise covariance matrix in the forward estimator for $\hat{\boldsymbol{x}}_k^*$ were adjusted using the current σ_{DSRC}^2.

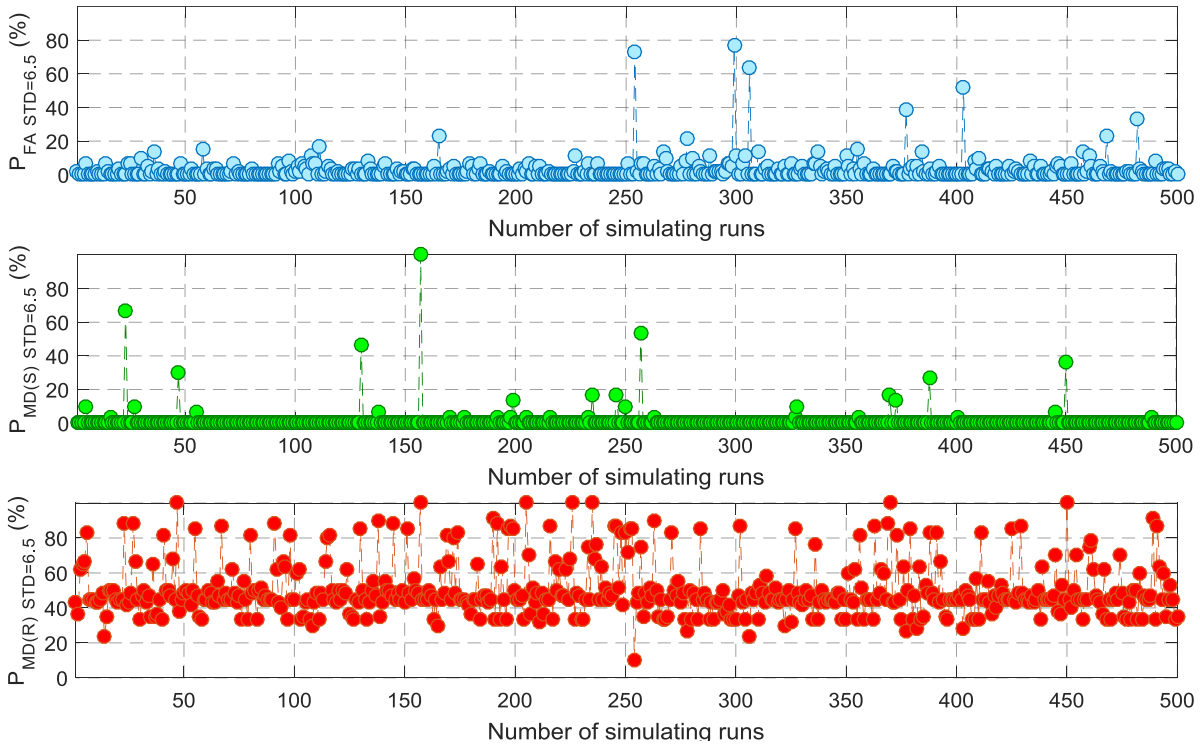

Figure 6. Statistical results of fault detection for 500 simulation runs (DSRC STD= 6.5)

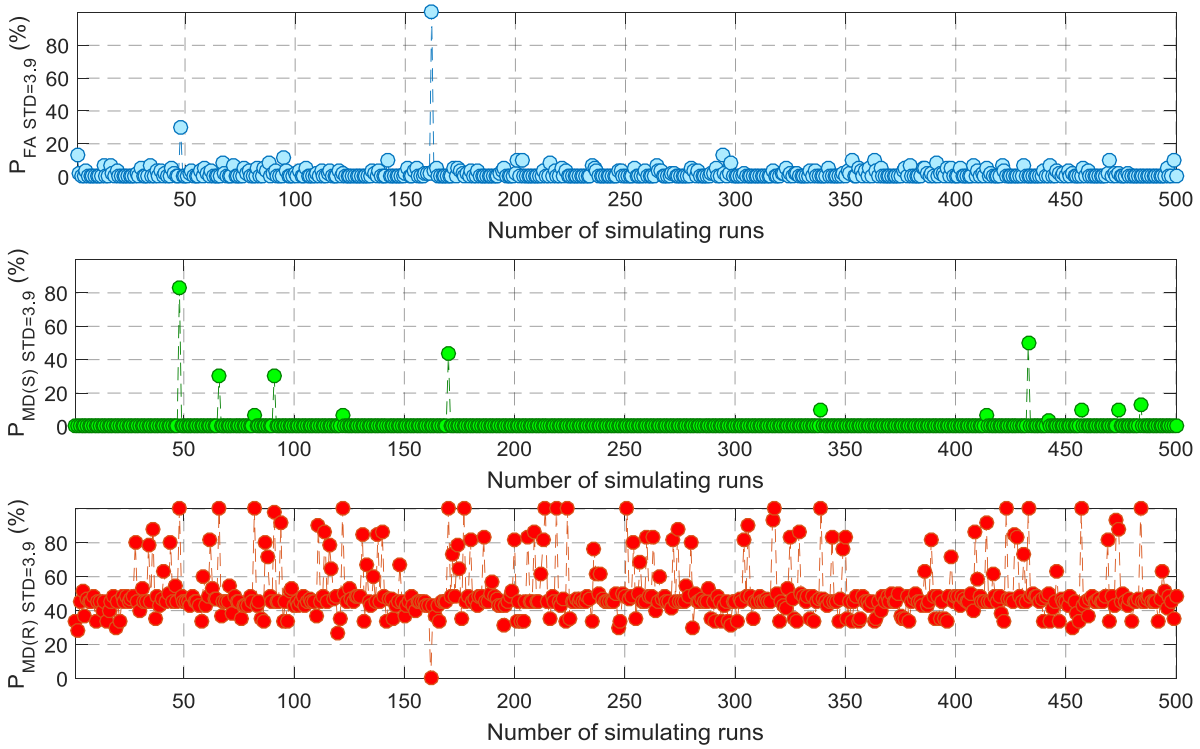

Figure 7. Statistical results of fault detection for 500 simulation runs (DSRC STD= 3.9)

Based on the statistical results from the simulations with different STD assumptions, it can be seen that the probabilities of false alarm and missed detection of the abrupt fault are not sensitive to DSRC range-rate error assumptions. Both the maximum percentage (7.03% for false alarm and 1.1% for missed detection) and the average (2.83% for false alarm and 0.36% for missed detection) illustrate a slight deviation in false alarm and missed detection rates (for ramp fault) under the simulated operation scenario. However, the percentage of missed detection of a soft fault varies among different DSRC STD assumptions. The missed detection

rate, with an average of 47.27% and a maximum value 52.79%, is much higher than that under the abrupt fault condition, which is accounted for by the assumption of a slowly growing ramp error and the difficulties in detection during an early period. A relatively low missed detection rate 41.21% is derived when an extreme small DSRC STD, which is only 10% of a nominal value 6.5m/s, adopted to establish virtual satellite observations for integrity monitoring. Under the 60-second ramp fault scenario with a ramp velocity of 1m/s, this missed detection rate represents an equivalent detectable threshold 24.73m for the pseudo-range errors. Compared to the maximum missed detection rate 52.79% when $\sigma_{\text{DSRC}} = 4.55$ is adopted, which indicates an equivalent detectable threshold 31.67m, this is an improvement of 21.91% when a small STD of DSRC range-rate error is assumed. In general, a lower variance of DSRC range-rate errors will contribute to the enhancement of integrity monitoring performance in detecting and excluding abrupt and ramp faults for the proposed DSRC-assisted cooperative integrity monitoring methodology.

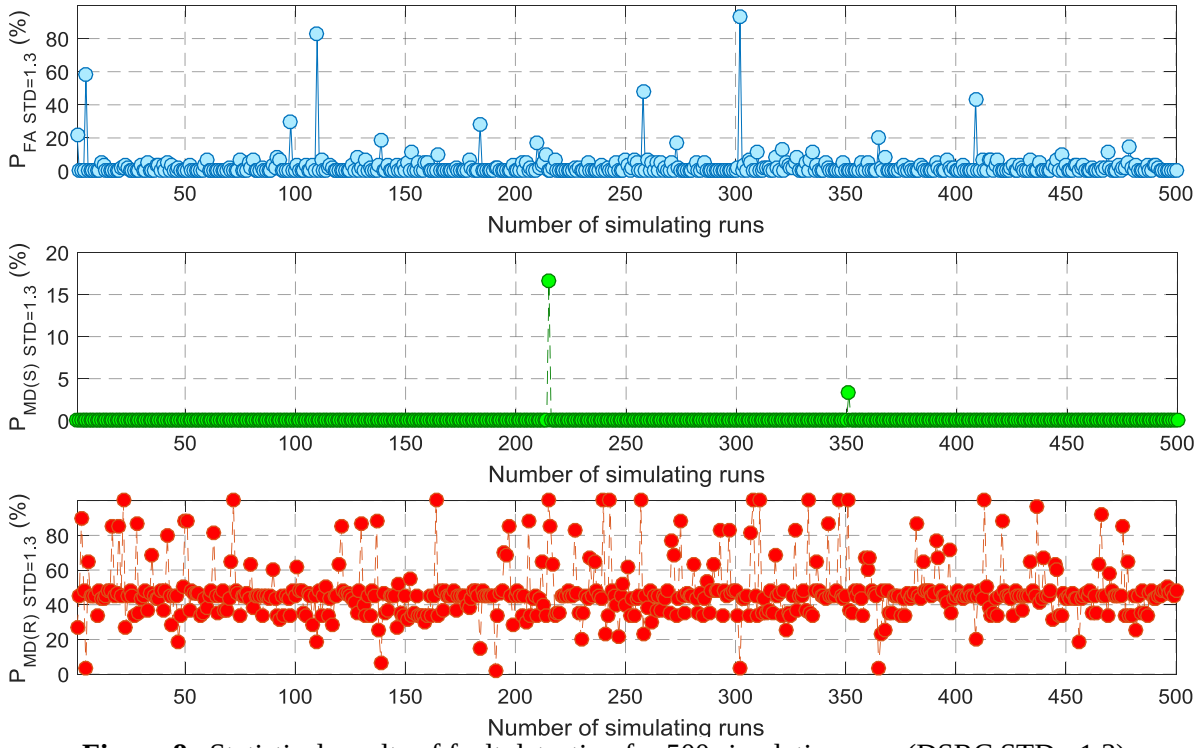

Figure 8. Statistical results of fault detection for 500 simulation runs (DSRC STD= 1.3)

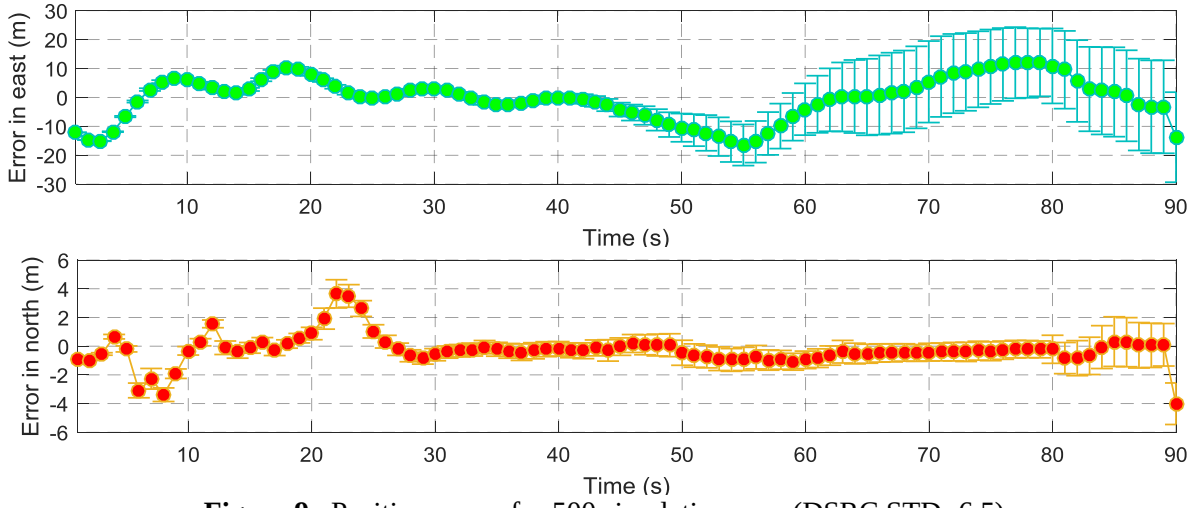

Figure 9. Position errors for 500 simulation runs (DSRC STD=6.5)

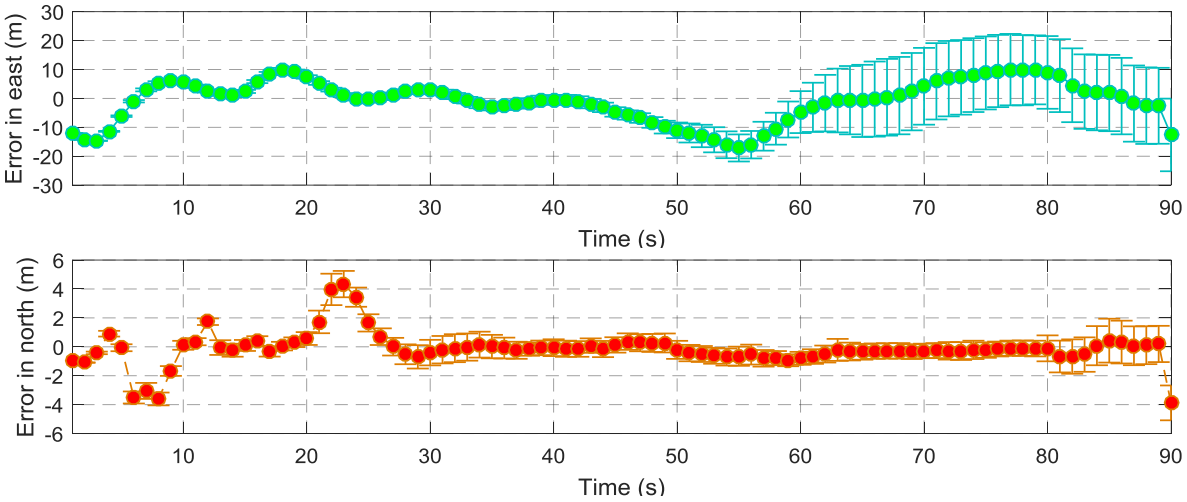

Figure 10. Position errors for 500 simulation runs (DSRC STD=3.9)

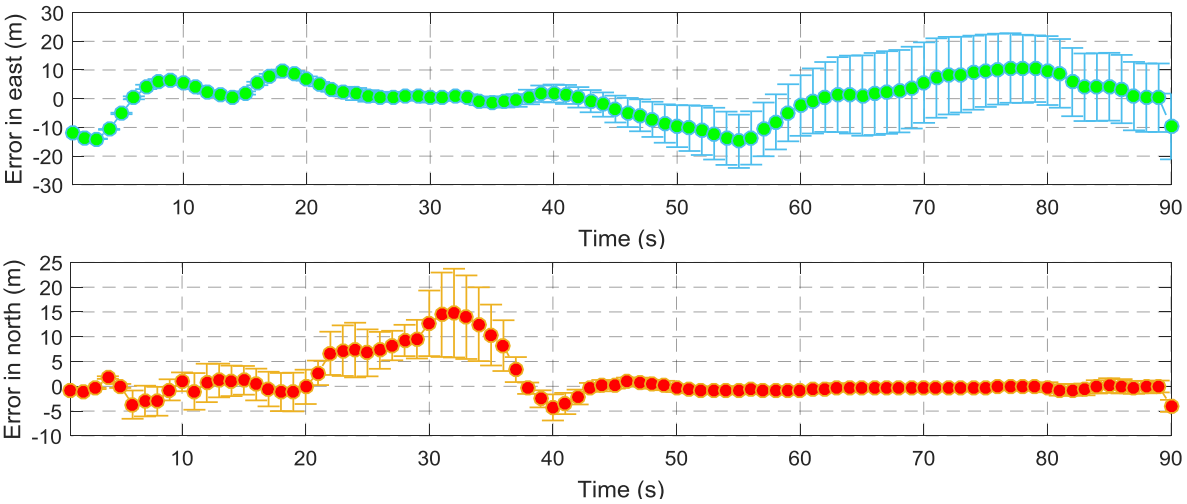

Figure 11. Position errors for 500 simulation runs (DSRC STD=1.3)

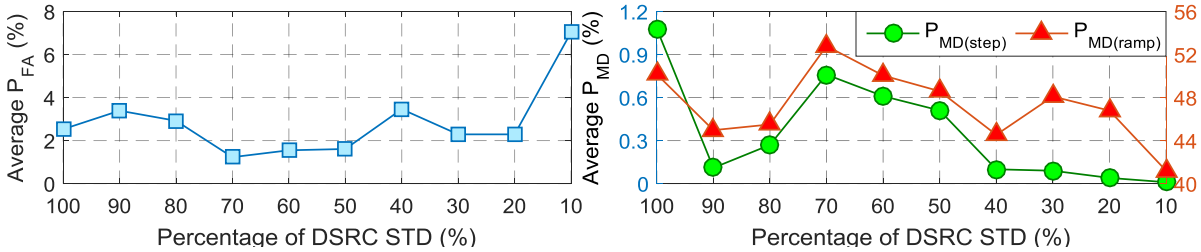

Figure 12. Comparison of fault detection results with different DSRC STD assumptions

Table 1. Fault detection with different DSRC STD assumptions

Ratio of STD_{DSRC}	100%	90%	80%	70%	60%	50%	40%	30%	20%	10%
μ (P_{FA}) (%)	2.53	3.39	2.92	1.23	1.55	1.61	3.46	2.29	2.29	7.03
μ (P_{MD_step}) (%)	1.08	1.1	0.27	0.76	0.61	0.51	0.10	0.09	0.04	0.01
μ (P_{MD_ramp}) (%)	50.16	44.97	45.50	52.79	50.05	48.59	44.54	48.1	46.79	41.21

There are several factors (as shown in Fig. 3) that influence the performance of cooperative integrity monitoring using DSRC as proposed in this paper. However, only the different assumptions of error characteristics of DSRC range-rate measurements have been considered. More investigations on the capabilities of the proposed integrity monitoring methodology and

the implementing strategies under different operational conditions have to be undertaken. It should be noted that the availability of integrity monitoring using the HPL-based criterion is not addressed in the simulations, as there is a lack of specifications in cooperative positioning for intelligent transport systems. This situation is quite different from aviation applications, however efforts and preliminary results are encouraging as far as implementing DSRC for both V2V and V2I communications and vehicle positioning solutions in the future.

5. CONCLUDING REMARKS

Previous studies on DSRC-enabled cooperative positioning for intelligent transport systems, the DSRC range-rate measurements have proven to offer potential in assisting GNSS positioning under a connected vehicles (VANET) environment, especially under difficult GNSS observation conditions. Based on traditional range comparison GNSS integrity monitoring methods using residual-enabled statistics, a virtual satellite pseudo-range generation strategy was presented based on DSRC measurements and road map data. The corresponding fault detection, identification and exclusion strategies were presented by considering the consistency between the virtual and observed pseudo-range measurements. The influencing factors for DSRC-assisted integrity monitoring have been summarised. The possibility of a higher accuracy level for DSRC-based range-rate measurements does enhance the performance of FDE. The proposed methodology was evaluated using simulated abrupt and soft faults, and the capability of detecting and identifying two parallel faults was investigated. Although only one major influencing factor, the nature of DSRC range-rate measurement error, has been investigated, the authors believe that the results are encouraging, and that a cooperative integrity monitoring scheme is feasible.

Our future work is focused on extending the fixed assumption of the DSRC CFO-based range-rate error model, as well as the simulated virtual satellite pseudo-range measurements, with Gaussian over-bound techniques by inflating variance of the assumed normal error model. More influencing factors rooted in the "DSRC-based virtual measurement generation" branch (see Fig. 3) will be investigated in order to evaluate the performance of the proposed DSRC-based integrity monitoring methodology and to derive suitable strategies for practical implementation. Moreover, field tests with DSRC units and commercial-grade GNSS receivers under varying operational conditions will need to be carried out. Finally, the adaptive capability of the cooperative integrity monitoring scheme against specific market conditions with different C-ITS penetration rates will be addressed via additional field tests and larger scale simulations.

ACKNOWLEDGEMENTS

This work was supported by Australian Research Council Discovery Project (DP 170103341) and Beijing Natural Science Foundation (4182053), under the support of the State Scholarship Fund by China Scholarship Council (CSC).

REFERENCES

Alam N, Balaei AT, Dempster AG (2011) A cooperative positioning method for VANETs using DSRC carrier frequency offset, *Proceedings of IGNSS Symposium*, Sydney, 1-11

Alam N, Balaei AT, Dempster AG (2013) Relative positioning enhancement in VANETs: a tight integration approach, *IEEE Transactions on Intelligent Transportation Systems*, 14(1): 47-55

Ansari K, Feng Y, Tang M (2015) A runtime integrity monitoring framework for real-time relative

positioning systems based on GPS and DSRC, *IEEE Transactions on Intelligent Transportation Systems*, 16(2): 980-992

Gu Y, Hsu L, Kamijo S (2017) Vehicle localization based on Global Navigation Satellite System aided by three-dimensional map, *Transportation Research Record*, 2621: 55-61

Karlsson R, Gustafsson F (2017) The future of automotive localization algorithms, available, reliable, and scalable localization: anywhere and anytime, *IEEE Signal Processing Magazine*, 34(2): 60-69

Lanca L, Romanovas M, Ziebold R (2017) On fault detection and exclusion in snapshot and recursive positioning algorithms for maritime applications, *European Transport Research Review*, 9(1): 1-15

Margaria D, Falletti E (2015) Proof-of-concept of the local integrity approach, *Proceedings of 2015 International Conference on Localization and GNSS (ICL-GNSS)*, Gothenburg, 1-6

Meng X, Roberts S, Cui Y, Gao Y, Chen Q (2018) Required navigation performance for connected and autonomous vehicles: where are we now and where are we going, *Transportation Planning and Technology*, 41(1): 104-118

Paden B, Cap M, Yong SZ, Yershov D, Frazzoli E (2016) A survey of motion planning and control techniques for self-driving urban vehicles, *IEEE Transactions on Intelligent Transportation Systems*, 1(1): 33-55

Shen F, Cheong JW, Dempster AG (2016) A DSRC Doppler/IMU/GNSS tightly-coupled cooperative positioning method for relative positioning in VANETs, *The Journal of Navigation*, 70(1): 120-136

Vivacqua RPD, Bertozzi M, Cerri P, Martins FN, Vassallo RF (2017) Self-localization based on visual lane marking maps: an accurate low-cost approach for autonomous driving, *IEEE Transactions on Intelligent Transportation Systems*, PP(99): 1-16 (On-line press)

Worner M, Schuster F, Dolitzscher F, Keller C, Haueis M (2016) Integrity for autonomous driving: a survey, *Proceedings of 2016 IEEE/ION Position, Location and Navigation Symposium (PLANS)*, Savannah, 666-671

Zhong L, Liu J, Li R, Wang R (2017) Approach for detecting soft faults in GPS/INS integrated navigation based on LS-SVM and AIME, *The Journal of Navigation*, 70(3): 561-579